The effect of secondary ice production parameterization on the simulation of a cold frontal rainband

Sylvia C. Sullivan[1,2], Christian Barthlott[1], Jonathan Crosier[3], Athanasios Nenes[2,4,5], and Corinna Hoose[1]

[1]Institute of Meteorology and Climate Research, Karlsruhe Institute of Technology, Karlsruhe, Germany
[2]Department of Chemical and Biomolecular Engineering, Georgia Institute of Technology, Atlanta, GA 30332, USA
[3]School of Earth, Atmospheric, and Environmental Studies, University of Manchester, Manchester, UK
[4]ICE-HT, Foundation for Research and Technology, Hellas, 26504 Patras, Greece
[5]Institute of Environmental Research and Sustainable Development, National Observatory of Athens, 15236, Palea Penteli, Greece

Correspondence to: S. Sullivan (scs2229@columbia.edu), A. Nenes (athanasios.nenes@gatech.edu), C. Hoose (corinna.hoose@kit.edu)

Abstract. Secondary ice production via processes like rime splintering, frozen droplet shattering, and breakup upon ice hydrometeor collision have been proposed to explain discrepancies between in-cloud ice crystal and ice-nucleating particle numbers. To understand the impact of this kind of additional ice number generation on surface precipitation, we present one of the first studies to implement frozen droplet shattering and ice-ice collisional breakup parameterizations in a larger-scale model.

5 We simulate a cold frontal rainband from the Aerosol Properties, PRocesses, And InfluenceS on the Earth's Climate campaign and investigate the impact of the new parameterizations on the simulated ice crystal number concentrations (ICNC) and precipitation. Near the convective regions of the rainband, contributions to ICNC can be as large from secondary production as from primary nucleation, but ICNCs greater than $50\,\mathrm{L^{-1}}$ remain underestimated by the model. Addition of the secondary production parameterizations also clearly intensifies the differences in both accumulated precipitation and precipitation rate between

10 the convective towers and non-convective gap regions. We suggest, then, that secondary ice production parameterizations be included in large-scale models on the basis of large hydrometeor concentration and convective activity criteria.

1 Introduction

Cloud microphysics mediate precipitation formation, either from the in-cloud liquid or ice phase. In both cases, precipitation is observed to form much faster than the time frame to form sedimentable hydrometeors by solely condensational or depositional growth. Instead, accretional growth is required, be it collision-coalescence of liquid droplets, droplet riming on ice hydrom-

15 eteors, or ice crystal aggregation. The efficiency of these processes is controlled by hydrometeor size through their terminal velocity and cross section within a collisional kernel (e.g., Rosenfeld and Gutman, 2001; Khain et al., 2005).

In clouds with high cloud condensation nuclei (CCN) concentrations, precipitation is more likely to initiate in the ice phase because cloud droplets will be smaller and less likely to grow to sedimentable size. This ice-initiated precipitation occurs often

20 over the continents, where aerosol loadings are higher (e.g., Mülmenstädt et al., 2015; Lohmann, 2017), and in convective clouds for which the vertical motions are strong enough to carry droplets above the freezing level. Cold phase initiation has

been associated with the top 10% of heavier rains according to data from the Tropical Rainfall Measuring Mission (Lau and Wu, 2011), and precipitation indices have been developed based upon cold cloud coverage (e.g. Arkin and Meisner, 1987; Joyce and Arkin, 1997). In these cases of ice-initiated precipitation, the requisite crystal growth can occur via the Bergeron process, in which water vapor transfers from droplets to ice crystals under appropriate thermodynamic conditions. Ice hydrometeors
5 eventually fall out of the cloud and reach an altitude at which they melt to form rain drops.

To accurately forecast cold phase-initiated precipitation, we must first accurately model in-cloud ice formation. Much effort has been devoted to understanding which atmospheric aerosols can act as ice-nucleating particles (INP) (e.g., Möhler et al., 2006; Knopf and Koop, 2006; Möhler et al., 2008; DeMott et al., 2010; Broadley et al., 2012; Hoose and Möhler, 2012; O'Sullivan et al., 2015; DeMott et al., 2016). But numerous measurements also indicate much larger in-cloud ice crystal
10 number concentrations (ICNC) than INP numbers (e.g., Crawford et al., 2012; Heymsfield and Willis, 2014; Lasher-Trapp et al., 2016; Taylor et al., 2016). These kinds of ICNC 'enhancements' may be due to shattering upon impact with the probe inlet (e.g., Heymsfield, 2007; McFarquhar et al., 2007), but more recent measurements employ probe tips that reduce airflow disturbance around the inlet (Korolev et al., 2013a, b) and interarrival time algorithms to filter out artifacts (Field et al., 2003, 2006; Korolev and Field, 2015). The ICNC-INP discrepancy remains in some cases, and a variety of secondary ice production
15 processes have been proposed to make up the difference.

Given the linkage of cloud ice and precipitation, including these secondary ice production processes in meteorological models may yield more accurate precipitation forecasts. But the precipitation change with ICNC change will not always be the same, as schematized in Figure 1. For example, an additional source of small ice crystals would extend cloud duration and delay precipitation in a kind of cloud lifetime effect. But the depositional growth of these small ice crystals may also deplete
20 supersaturation to a level at which the Bergeron process initiates. Then ice hydrometeors quickly become large, shortening cloud duration and accelerating precipitation. A 'cascade effect' has been proposed in which small ice crystals collide with large droplets, freezing and shattering them and forming more crystals (Lawson et al., 2015). Or dynamic-microphysical feedbacks could exist: an additional source of small crystals would generate more latent heat, changing the vertical heating profile and potentially affecting precipitation through altered detrainment rates or cloud updrafts (e.g. Clark et al., 2005). Along
25 with the hydrological implications of altered precipitation, more glaciated clouds will be optically thinner and radiatively warm the surface.

Several studies have considered these linkages, both with measurements and models, but no consensus has been reached on their individual or net impacts. For example, Connolly et al. (2006) did not see a large change in surface precipitation from a tropical thunderstorm when they altered the rime splintering rate in the Weather Research and Forecasting model.
30 Dearden et al. (2016) also found that, in simulations of summertime cyclones, depositional growth of ice crystals was much more influential than inclusion of rime splintering on the spatial distribution of precipitation. On the other hand, an early study by Aleksić (1989) found that, in Serbia, more numerous ice crystals due to a hail suppression program led to more intense rainfall. Clark et al. (2005) discussed how the latent heating from additional ice generation modifies the vertical temperature profile, and hence precipitation rates. And Taylor et al. (2016) concluded that the combination of droplet coalescence and
35 secondary ice production often determined precipitation timing and intensity in the maritime cumuli they observed. The kind
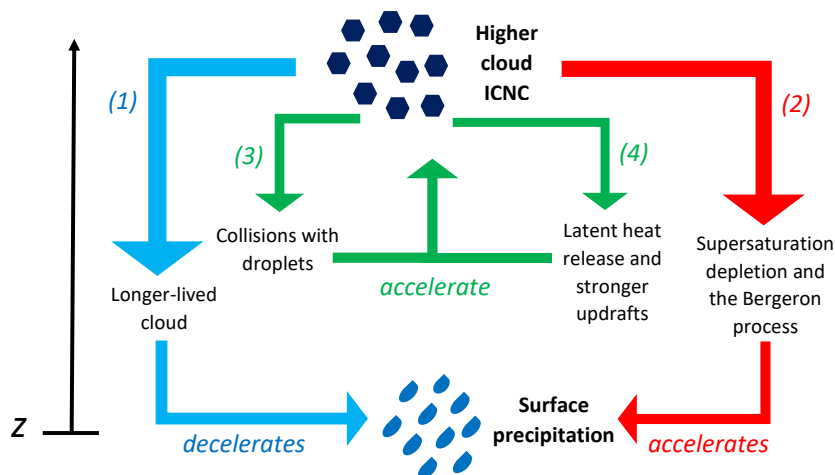
Figure 1. Secondary production will generate higher ICNCs within mixed-phase clouds, but different feedbacks and impacts on precipitation are possible. Precipitation rates could decelerate via a cloud lifetime effect (1), where small crystals stay aloft longer, or accelerate via supersaturation depletion (2), where larger crystals grow at the expense of liquid droplets via the Bergeron process. Additional crystals could also collide, freeze, and shatter droplets in a cascade effect (3) or strengthen the updraft and supersaturation via their release of latent heat of fusion (4).

of compensating effects discussed above, along with the insusceptibility of accretional processes to aerosol perturbations, would also reduce sensitivity of precipitation to aerosol more generally, as discussed in the study of Glassmeier and Lohmann (2016).

   In this study, we implement parameterizations of frozen droplet shattering and ice-ice collisional breakup, two proposed

5 secondary production processes, into the Consortium for Small-Scale modeling (COSMO) framework described in Section 3. Frozen droplet shattering refers to a pressure build-up as a larger droplet freezes, either due to formation of an external ice shell or to latent heat of fusion release. This increased pressure eventually leads to spicule ejection or cracking and explosion of the ice shell (Leisner et al., 2014; Wildeman et al., 2017). In ice-ice collisional breakup, the impact of two ice hydrometeors leads to shattering, particularly of dendrites or fragile protuberances (Vardiman, 1978; Takahashi et al., 1995; Yano and Phillips, 2011).

10 COSMO already includes a description of a third process called rime splintering (Hallett and Mossop, 1974). We investigate the impact of these parameterizations on the simulated ICNC and surface precipitation in a case study.

2 Parameterizations

2.1 Frozen droplet shattering parameterization

Recent droplet levitation experiments of Leisner et al. (2014) and high speed video from Wildeman et al. (2017) are elucidating the exact physics behind the shattering of droplets as they freeze. For now, we parameterize this process with the product of a
5 fragment number, a temperature-dependent shattering probability, and the existing droplet freezing tendency:

$$\frac{\partial N_{ice}}{\partial t}\bigg|_{DS} = \Big[1 + p_{DS}\aleph_{DS}\Big]\frac{\partial N_{freez}}{\partial t} \tag{1}$$

$$p_{DS} = \frac{p_{max}}{\max\{\mathcal{N}(T_\mu,\sigma)\}}\mathcal{N}(T_\mu,\sigma) \tag{2}$$

$$\mathcal{N}(T_\mu,\sigma) = \frac{1}{\sqrt{2\pi}\sigma}\exp\Big[\frac{-(T-T_\mu)^2}{2\sigma^2}\Big] \tag{3}$$

We use a constant value for the ejected fragment number $\aleph_{DS}$ because measurements of this value are ongoing. Future studies
10 should add dependency on droplet size and perhaps temperature to this parameter. Shattering probability is given by a normal distribution in temperature, centered at a temperature T_μ of 258 K, with a default standard deviation σ of 3 K and default maximum probability p_{max} is 20% similar to Sullivan et al. (2018). Examples of this distribution are shown in Figure 2b and d. Then $\partial N_{freez}/\partial t$ is the number of frozen raindrops for a given time step, predicted by the Bigg (1953) heterogeneous freezing parameterization (see Appendix A for details).

15 ### 2.2 Ice-ice collisional breakup parameterization

Breakup upon ice hydrometeor collision is parameterized as the product of a fragment number generated upon collision and the existing hydrometeor collision tendency:

$$\frac{\partial N_{ice}}{\partial t}\bigg|_{BR,jk} = -\aleph_{BR}\frac{\partial N_j}{\partial t}\bigg|_{coll,jk} \tag{4}$$

$$\aleph_{BR} = F_{BR}(T - T_{min})^{1.2}\ \exp\Big[-(T-T_{min})/\gamma_{BR}\Big] \tag{5}$$

$$\frac{\partial N_j}{\partial t}\bigg|_{coll,jk} = -\frac{\pi}{4}\overline{E_{jk}}N_j N_k\big[\delta_j^0 D_j^2(\overline{x_j}) + \delta_{jk}^0 D_j(\overline{x_j})D_k(\overline{x_k}) + \delta_k^0 D_k^2(\overline{x_k})\big] \tag{}$$

$$\times [\theta_j^0 v_j^2(\overline{x_j}) - \theta_{jk}^0 v_j(\overline{x_j})v_k(\overline{x_k}) + \theta_k^0 v_k^2(\overline{x_k})]^{1/2} \tag{6}$$

where the number of fragments generated $\aleph_{BR}$ is based upon the laboratory data of Takahashi et al. (1995) as in Sullivan et al. (2017). Within Equation 5, T_{min} is a minimum temperature below which no breakup occurs and γ_{BR} is the decay rate of fragment number at warmer subzero temperatures. The effect of these parameters, along with the leading coefficient F_{BR}, is
25 illustrated in Figure 2a and c. The collisional tendency $\partial N_j/\partial t_{coll,jk}$ involves a collection efficiency E_{jk}; the number, mass,

Table 1. New subroutines in the two-moment scheme, containing the ice hydrometeor collision parameterizations, given as *collider_ breakup_ collided*.

	ice crystals	snow	graupel	hail
ice crystals			*graupel_ breakup_ ice*	*hail_ breakup_ ice*
snow			*graupel_ breakup_ snow*	
graupel	*graupel_ breakup_ ice*	*graupel_ breakup_ snow*		*hail_ breakup_ graupel*
hail	*hail_ breakup_ ice*		*hail_ breakup_ graupel*	

and terminal velocities of the colliding hydrometeors; and nondimensional values δ^0 and θ^0 from a gamma size distribution (see Appendix B for details). The parameterization works with four ice hydrometeor classes, shown in Table 1, by designating one hydrometeor class as the 'collider' (j) and a second as the 'collided' (k). The number in the 'collided' class is increased by $\aleph_{BR}$, while that in the 'collider' class remains constant. Mass in both classes remains unchanged. Future studies could include

5   collisions between all hydrometeor classes or redistribute number and mass between the 'collider' and 'collided' differently. These considerations could also be obviated by implementing the parameterization within a property-based ice microphysics scheme like the Predicted Particle Properties (P3) scheme (Morrison and Milbrandt, 2015; Milbrandt and Morrison, 2015). P3 tracks ice mixing ratio, number, mass, and rime fraction rather than number and mass in snow, graupel, and ice crystal categories whose thresholds can be non-physical.

10   **2.3   Rime splintering parameterization**

The existing parameterization of rime splintering is a product of a leading coefficient, a temperature-dependent weighting, and a rime mixing ratio:

$$\left.\frac{\partial N_{ice}}{\partial t}\right|_{RS} = \aleph_{RS} w_{RS} q_{rim}. \tag{7}$$

A default value of 3.5×10^8 fragments per kilogram of rime, $\aleph_{RS}$, is used base on the experiments of Hallett and Mossop

15   (1974). w_{RS} denotes a temperature-dependent weighting for rime splintering, which is triangular between 265 and 270 K by default and shown in Figure 2a and b. Several other options for this temperature weighting have been added and are shown in Figure 2e: a shifted triangular weighting between 255 and 260 K (**SH**); two broadened ones between 255 and 270 K (**BR1** and **BR2**); a symmetric one centered at 262 K (**SH**); and a uniform one between 255 and 273 K (**UNI**). Although observations indicate that rime splintering occurs at warm subzero temperature, primarily above 265 K, we are interested in capturing any

20   kind of cascade effect, as mentioned above. One can imagine a scenario in which even minimal rime splintering generates enough ice to collide with droplets, freezing and then shattering them. These splinters could then go on to collide with, freeze, and shatter other droplets in a runaway cloud glaciation.

Table 2. Sensitivity tests are listed with $\aleph_{RS}$ in units of (mg rime)$^{-1}$ and T_{min}, σ in units of K; results from runs enclosed in parentheses are not visualized.

		Droplet shattering				**Ice-ice collisional breakup**			
Set 1A	**1Ag**:	$\aleph_{RS} = 3000$,	$w_{RS} = $ UNI		*Set 2B*	**2Big**:	*graupel_breakup_ice*		
	1Ac:	$\aleph_{RS} = 300$,	$w_{RS} = $ SH			**2Bgh**:	*hail_breakup_graupel*		
	1Am:	$\aleph_{RS} = 850$,	$w_{RS} = $ SY			**2Bih**:	*hail_breakup_ice*		
	1An:	$\aleph_{RS} = 3000$,	$w_{RS} = $ SH			**2Bsg**:	*graupel_breakup_snow*		
Set 3A	**3Ag**:	$p_{max} = 40\%$,	$\aleph_{DS} = 100$,	$\sigma = 12$	*Set 3B*	**3Bg**:	$F_{BR} = 360$,	$T_{min} = 249$	$\gamma = 5$
	3Ac:	$p_{max} = 5\%$,	$\aleph_{DS} = 2$,	$\sigma = 3$		**3Bc**:	$F_{BR} = 40$,	$T_{min} = 257$	$\gamma = 3$
	3Am:	$p_{max} = 10\%$,	$\aleph_{DS} = 10$,	$\sigma = 7$		**3Bm**:	$F_{BR} = 180$,	$T_{min} = 256$	$\gamma = 3$
	3An:	$p_{max} = 25\%$,	$\aleph_{DS} = 100$,	$\sigma = 3$		**3Bn**:	$F_{BR} = 500$,	$T_{min} = 258$	$\gamma = 1.5$

Finally, we limit rime splintering to occur only after collisions between raindrops and ice crystals, graupel, or hail, assuming that the smaller size of cloud droplets and the slower terminal velocity of snow do not lead to the fragile frozen protuberances that easily splinter (e.g., Choularton et al., 1980; Mossop, 1985).

3 Simulations

5 These parameterizations and adjustments are implemented into the Consortium for Small-Scale modeling (COSMO) framework version 5.03 (Baldauf et al., 2011; Doms and Baldauf, 2015) that employs the two-moment microphysics scheme of Seifert and Beheng (2006). Several sensitivity tests are run, as listed in Table 2 and visualized in Figure 2. Simulation names include an 'A' if they employ the droplet shattering parameterization and a 'B' if they employ the ice-ice collisional breakup one. Set 1 adjusts the fragment number formed per milligram of rime $\aleph_{RS}$ within the rime splintering parameterization; Set

10 2 adjusts the ice hydrometeor classes that collide; and Set 3 adjusts the parameters within the collisional breakup parameterization. For each simulation, an ensemble of 10 runs is done with "stochastically perturbed physics tendencies" (e.g., Buizza et al., 1999), applied to vapor, cloud, and ice mixing ratio tendencies, and the ensemble mean output and standard deviation are evaluated. A control simulation with the standard Seifert and Beheng microphysics scheme is also run and denoted 'CTRL' throughout.

15 We use these parameterization configurations to simulate 3 March 2009 for a domain centered at 53°N, 5°W, with longitudes ranging from 65°N down to 46°N and latitudes ranging from 18°W to 10°E. In-situ cloud ice data and remote-sensing rainfall
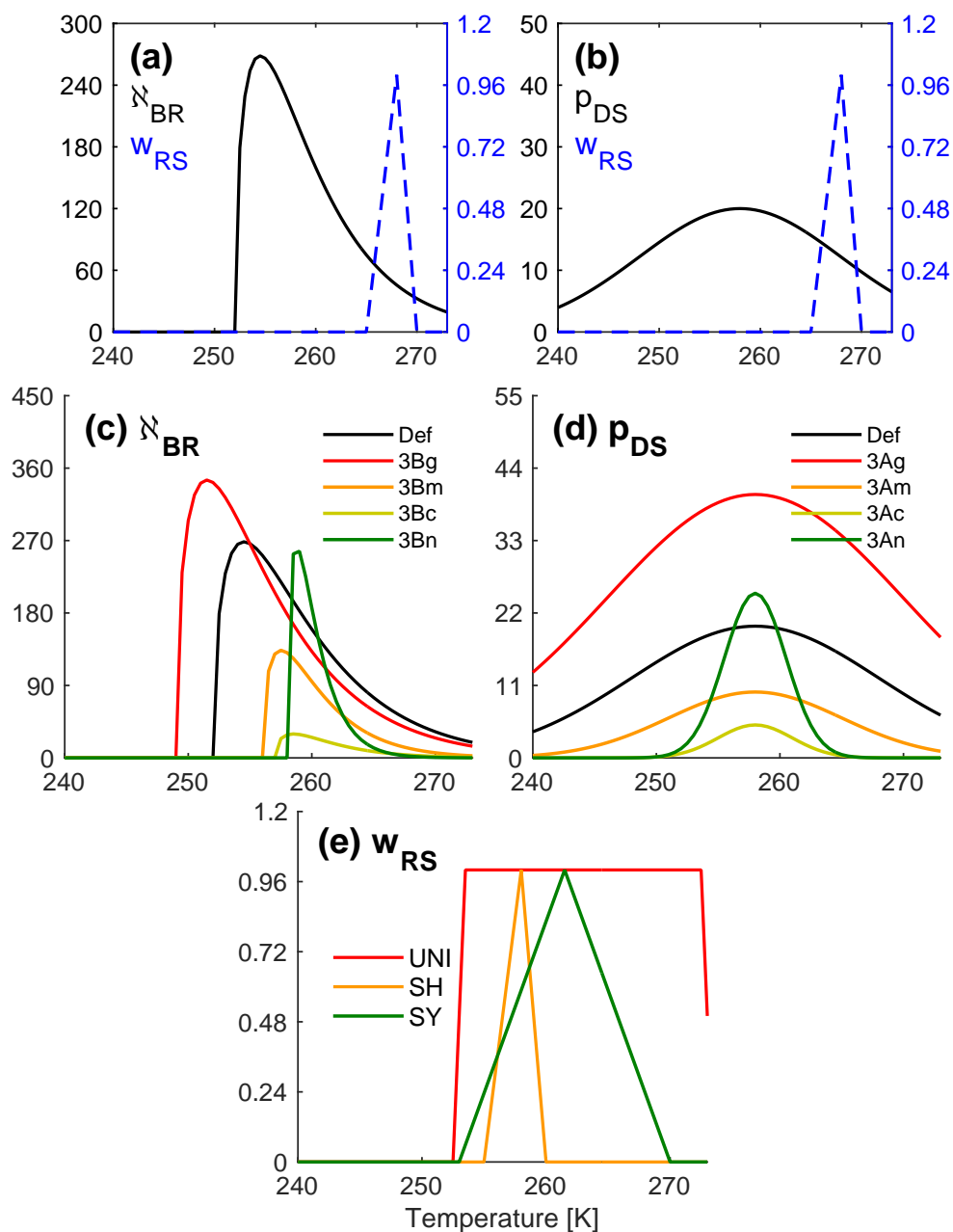
Figure 2. Fragment numbers, weightings, and probabilities from the secondary ice production parameterizations. The default fragment number from ice-ice collisional breakup $\aleph_{BR}$ (used in Set 2B) and rime splintering weighting w_{RS} are shown in panel (a) versus temperature. Panel b shows w_{RS} again, overlapping the probability of a frozen droplet shattering p_{DS} (used in Set 1A), in percent. The various $\aleph_{BR}$ functions used in the Set 3B simulations are shown in panel (c); the various p_{DS} functions in Set 3A in panel (d); and the various w_{RS} functions in Set 1A in panel (e).

data are available for this case from the Aerosol Properties, PRocesses And InfluenceS on the Earth's climate (APPRAISE) campaign and Chibolton Facility for Atmospheric and Radio Research (CFARR) in Southern England respectively. The observations showed the passage of a narrow cloud frontal rain band over the UK around 1800 UTC and CFARR at 2000 UTC. These data have been thoroughly analyzed by Crosier et al. (2014).

5   The COSMO interpolation utility (INT2LM) was used to construct initial and boundary conditions from the 7-km COSMO-EU operational assimilation cycle analyses. All simulations are done at 2.8 km spatial resolution with a time step of 25 seconds, 50 vertical levels, and half-hourly output resolution. The Aerosol and Reactive Trace gases module (ART) is turned off. The Phillips et al. (2008) parameterization is used for primary ice nucleation, and the intermediate CCN level of the Segal and Khain parameterization is applied (Segal and Khain, 2006).

10   The rainband structure allows us to investigate multiple secondary production processes at the same time because it contains regions with varying dynamic and thermodynamic conditions. For example, large liquid water contents and stronger updrafts are favorable for frozen droplet shattering (Lawson et al., 2015; Taylor et al., 2016), and these conditions can be found in the narrow leading edge. For rime splintering, lower updrafts and liquid water contents and bimodal droplet size distributions are favorable (e.g. Choularton et al., 1980; Mossop, 1985; Heymsfield and Willis, 2014), and these conditions are found at the top

15 of convective turrets and in the trailing region of stratiform precipitation. The rainband vertically spans the optimal temperature zones for both droplet shattering and rime splintering (Hallett and Mossop, 1974; Leisner et al., 2014; Lawson et al., 2015) and horizontally spans both maritime and continental zones to compare any impact of different surface heat budget.

4   Results

4.1   Impact on ice crystal production

20 We first present the spatial fields of secondarily-produced ICNC, $N_{i,sec}$, and these values relative to the primarily-nucleated ICNC, $N_{i,pri}$, at a single pressure level in Figure 3. The pressure level is chosen to maximize this $N_{i,sec}$, and simulations 1Ag and 1Ac are shown with both frozen droplet shattering and rime splintering at different $\aleph_{RS}$ and w_{RS}. The 1Am and 1An simulations contain intermediate values and are not shown. $N_{i,sec}$ is an accumulated ICNC from the secondary production processes between 1800 and 1900 UTC, as the cold frontal rainband begins to pass over the UK, and does not include any

25 sedimentation loss to lower levels to gain from higher ones. The characteristic comma shape of clouds within a well-developed mid-latitude cyclone is apparent in panels a and b, and ICNC of up to 10^5 L^{-1} are produced over the half hour. The structure in $N_{i,sec}$ follows the rainband structure because it is contingent upon the large hydrometeors formed in the convective regions. Particularly for the rime splintering, mixing of young and old thermals at the top of convective towers may generate the bimodal droplet size distribution that seems to make the process more efficient (Mason and Jonas, 1974; Korolev, 1994).

30   In the 1Ac simulation, however, the large values of $N_{i,sec}$ are found not only in the rainband region, but also over Ireland and the adjacent North Atlantic. In fact, the spatial extent of large $N_{i,sec}$ is greater with the more conservative 1Ac simulation than the 1Ag one with larger $\aleph_{RS}$ and w_{RS}. A uniform temperature weighting in 1Ag allows the secondary ice generation to occur over more altitudes, so that the remaining rime mixing ratio in the air reaching this pressure level in the 1Ag simulation
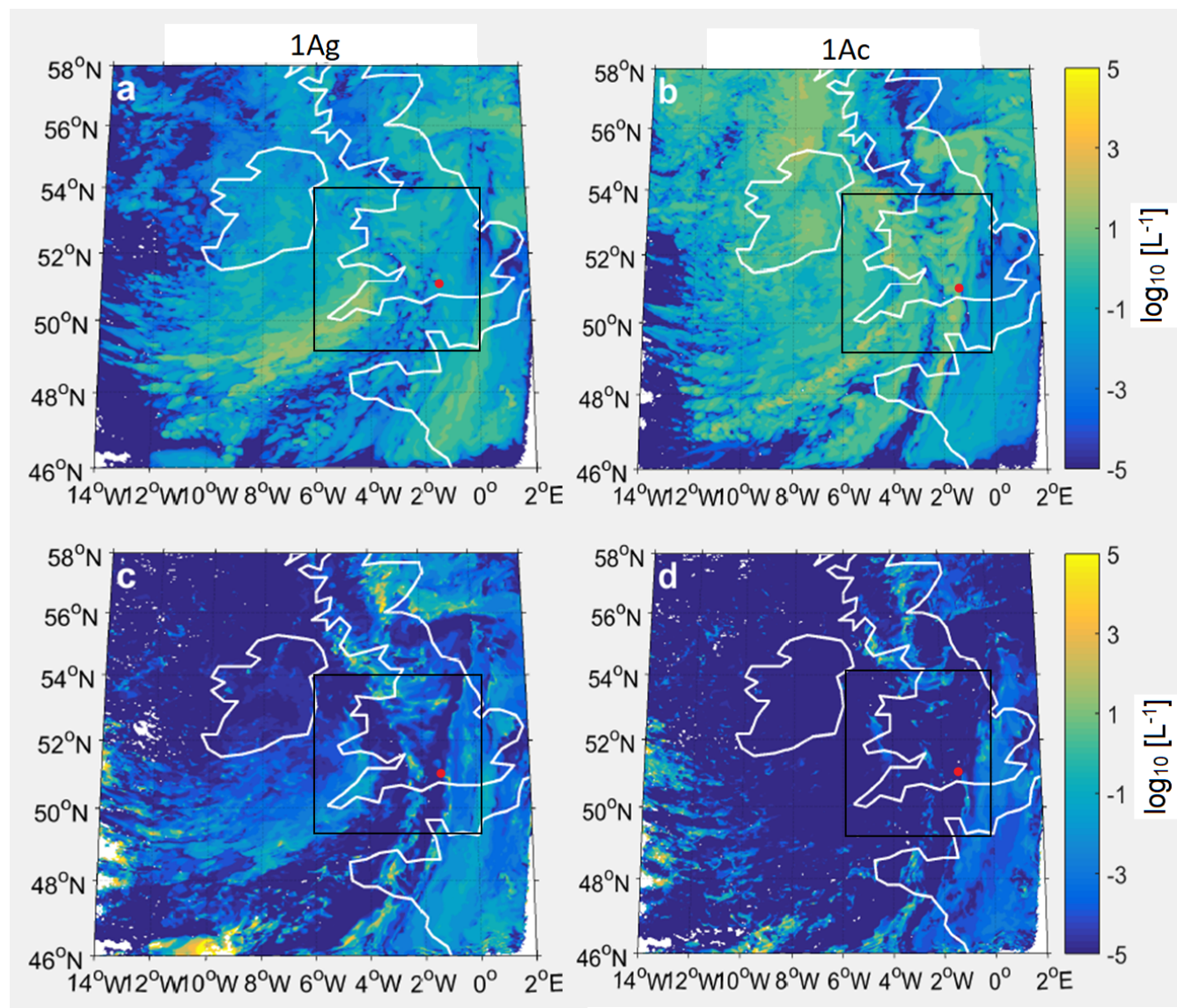
Figure 3. Maps of secondarily-produced ice from the 1Ag (on the left) and 1Ac (on the right) simulations at the pressure levels where $\overline{T} \approx$ 258 K, as the rainband began to pass over the UK. Panels a and b show the number of secondarily-produced ice crystals from 1800 UTC to 1900 UTC, and panels c and d show the ratio of secondarily-produced to primarily-nucleated ICNCs for the same time period. The black box shows the subdomain used in Figure 4, and the red dot is the CFARR location.

may be somewhat lower than that in the 1Ac simulation. While the total horizontal extent of large $N_{i,sec}$ is greater in 1Ac than in 1Ag, the production region right around the rainband is more defined: in regions of high liquid water content, the rime mixing ratio is unlikely to be depleted and the 1Ag simulation does indeed produce higher $N_{i,sec}$.

Adjustments to the spatial distribution of ice formation will have energetic implications. If secondary ice production occurs
5   over a great altitudinal depth, the small ice crystals are more likely to be advected into an outflow region where they will contribute to cirrus optical thickening and warming. Crosier et al. (2014) note the fallstreaks at cloud top of this rainband in their Doppler radar measurements. There are not heating effects directly associated with the rime splintering process. But higher ICNCs do make droplet riming more likely, so an indirect effect from heat of fusion release exists. Zhu et al. (2017) recently showed that melting over a greater depth strengthens the vertical advection of moisture, so it might be expected that freezing
10 over greater depth would suppress this vertical moisture transport. But existing studies indicate that more intense detrainment may be the more important effect from freezing (Sud and Walker, 2003). Varying aerosol concentrations and surface radiative budgets over continental versus maritime environments could also affect ICNC. For example, secondary production should be less likely over continental regions with higher aerosol loadings because more and smaller cloud droplets form, diminishing the riming and droplet freezing efficiencies. In this case, however, no notable differences appear in the spatial snapshots of
15 Figure 3.

To gauge the importance of including these additional ice sources, $N_{i,sec}$ accumulation can be compared to $N_{i,pri}$. In panels c and d, $N_{i,sec}/N_{i,pri}$ ranges from 0.1 to 10, particularly in the simulation with higher $\aleph_{RS}$ and w_{RS}. The higher values of the ratio occur in the wide, trailing region of the rainband and in the 1Ag simulation, but still in a limited region. In simulations with ice-ice collisional breakup (not shown), $N_{i,sec}$ is 100-fold smaller and the $N_{i,sec}/N_{i,pri}$ ratio is less than one in all regions. The
20 liquid-dependent secondary production processes are more important in the case of the rainband, given the prevalence of large droplets and relative absence of either graupel or hail (Crosier et al., 2014). A means of including secondary ice production in larger-scale models, then, could be to include the parameterizations on the basis of large hydrometeor number criteria: the droplet shattering and collisional breakup parameterizations could be turned on within the microphysics scheme only for those cloudy grid cells with greater than a certain concentration of large droplets and graupel, hail, or snow respectively.

25 Along with the spatial field, we show the altitudinal, probability, and temporal distributions of modeled and observed ICNC in Figure 4. In panel a, we compare the vertical profiles of ICNC in pressure coordinates from 1800 to 2100 UTC and in a sub-domain centered at CFARR (49° to 54°N latitude and from 6°W longitude to the Prime Meridian). Modeled values were output for pressures from 100 to 900 hPa at 50 hPa intervals, and observations from a clouding imaging probe CIP-15 are discretized into the largest number of pressure bins that still give reliable statistics. The envelopes on all profiles represent the
30 first and third quantiles of ICNC in the interval or bin. Simulated values less than 0.01 m^{-3} are filtered out.

At the higher altitudes and colder temperatures, the modeled ICNCs all overlap because they use the same representations of heterogeneous and homogeneous ice nucleation. Both the simulated median and standard deviation are also in good agreement with the CIP-15 observations. Then at the lowest altitudes and warmest temperatures, the 1Ag simulation is the only one to match the observations well. In fact, the observed and modeled median ICNCs between 800 and 850 hPa are within 30% of
35 one another, indicating the rime splintering process at these warmer subzero temperatures is well-captured by a more generous

temperature weighting and fragment number parameter. Inclusion of ice-ice collisional breakup also brings ICNC closer to the observed values in the 3Bg simulation, but the values remain about an order of magnitude too small. The control simulation in red generates by far the fewest crystals, two orders of magnitude less than the observations between 800 and 850 hPa.
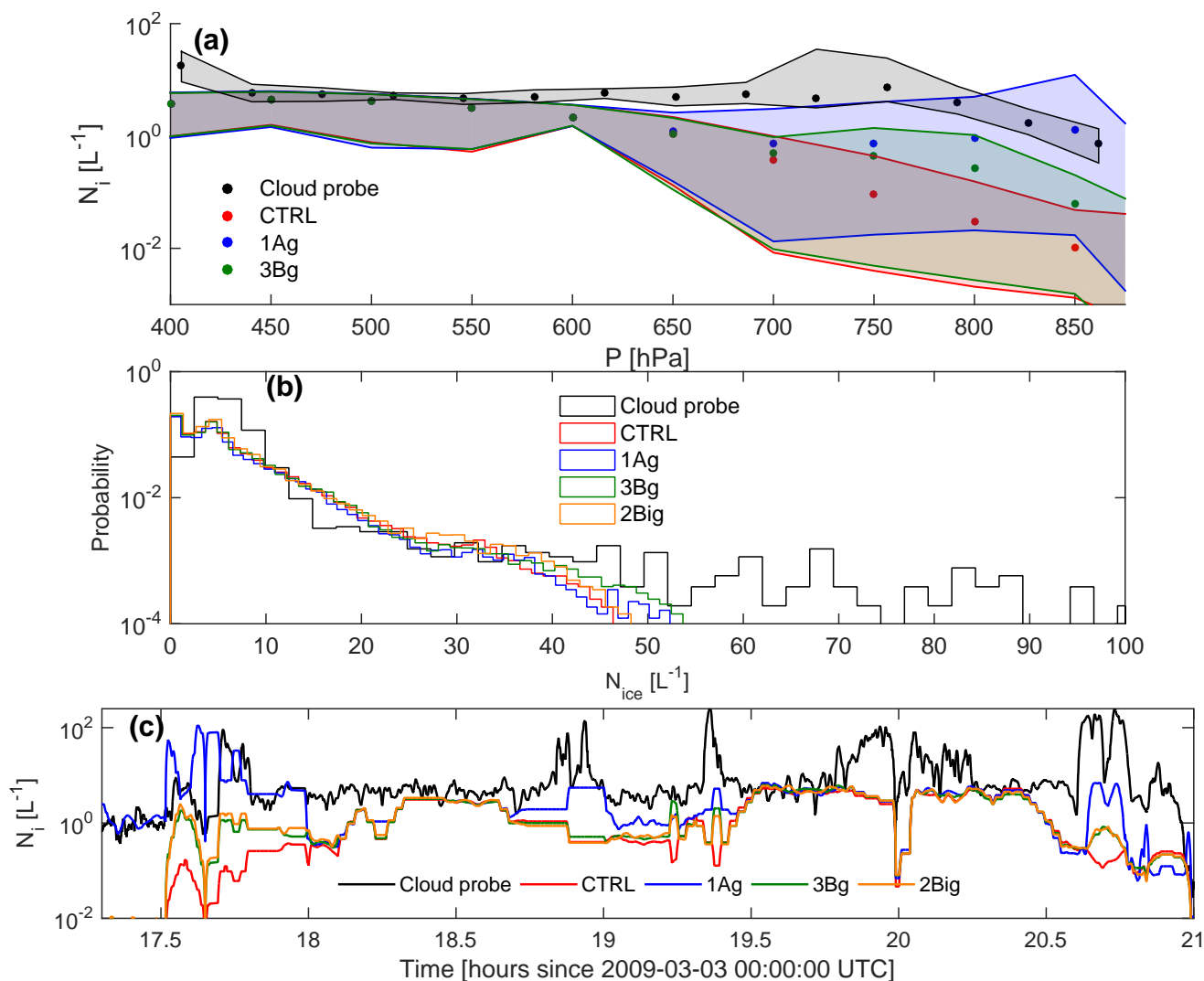
Figure 4. Various distributions of APPRAISE CIP-15 observed and simulated ICNC between 1700 and 2100 UTC for a small domain centered at CFARR with logarithmic scales. Panel a shows altitudinal profiles, where the dotted values indicate median, while the upper and lower envelopes show the first and third quantiles. Panel b shows probability distributions and panel c shows the 30-point running mean time series. Euclidean distance is minimized to find simulated values that correspond to the observed ones in the time series.

At intermediate altitudes, between 600 and 750 hPa, the observations fall above all the simulated ICNCs, even the upper quantile of the 1Ag simulation. This altitudinal range has a temperature around 258 K, where p_{DS} and $\aleph_{BR}$ are maximal, but

the underestimation suggests that the parameterizations remain too conservative or that multiple processes are active simultaneously. Indeed, in their study of cumuli in the same Southwestern Peninsula region, Taylor et al. (2016) find that combinations of secondary production processes are necessary to explain observed ICNCs. Graupel and hail were not present in large quantities during this case, but a peak in the hydrometeor size profile at 4 km suggests snow formation there (Crosier et al., 2014).

5 It is also possible then that including snow-snow collisions in Table 1 would bring ICNC into better agreement with the CIP-15 measurements.

In panel b, we show the ICNC probability distributions from cloud probe observations (in black) and the control, 1Ag, 3Bg, and 2Big simulations (in color) between 1800 and 2100 UTC and between 650 and 850 hPa. Values come again from the subdomain centered at CFARR. The simulated and observed distributions vary strongly in their higher order moments.

10 The observed distribution is far more skewed with a long tail out to N_{ice} of 100 L^{-1} and has a higher kurtosis as the larger probabilities at low N_{ice} drop off quickly. The simulated distributions drop off more quickly with negligible probabilities by about 45 L^{-1}, and their kurtosis is larger, as the high probabilities at low N_{ice} drop off only slowly through the intermediate values. The probability of small N_{ice}, less than 1 L^{-1} is still much higher in simulations than observations, although values of less than 10^{-3} L^{-1} have been filtered out. At these lower concentrations, however, measurements will be less precise

15 because of sampling volume and flow rate limitations, and model output is more susceptible to numerical noise. The simulation distributions themselves overlap strongly, but differences are present at 35 L^{-1} and above. By concentrations of 45 L^{-1}, only the 1Ag and 3Bg simulations have non-negligible probabilities.

Finally, we look at the temporal evolution of N_{ice} in both observations (in black) and the control, 1Ag, 3Bg, and 2Big simulations (in color) in panel c. To collocate a simulated value with the observed one at a given time, we use the grid cell that

20 minimizes the Euclidean distance to the latitude, longitude, and altitude where the measurement was made. In some instances then, for example between about 1815 and 1835 UTC, a simulated value is reused because the aircraft circled the same location.Thereafter a thirty-point running mean is calculated for all series. The underestimate in the simulations is apparent again, although it is by far the least for the 1Ag simulation, as in the altitudinal profiles of panel a. The observed trends – sudden increases around 1730 UTC, right before 1930 UTC, and after 2030 UTC or the sudden decrease at 2000 UTC–

25 appear also in the simulated time series. But the ICNC magnitude is always closest to observations in the 1Ag simulation with droplet shattering, followed by the 3Bg and 2Big ones with collisional breakup. The control simulation without secondary ice always has the largest discrepancy from cloud probe values. So although simulated ICNC remains too low, the secondary ice parameterizations do consistently shift the values in the right direction.

4.2 Impact on precipitation

30 Changes in the spatial and temporal distributions of ICNC are expected upon addition of another ice generation mechanism. But the new parameterizations may also have an indirect impact on other metrics. In particular, we consider adjustments to the spatial distributions of accumulated precipitation P_{tot} and of precipitation rate $\dot{P}$. In Figure 5, P_{tot} is shown for a small domain near CFARR at 1800 UTC, as the rainband begins to pass over the UK. Panel a shows values from the control simulation, which can already be as high as 30 mm in the first continental regions over which the rainband passes. Larger accumulated rainfall
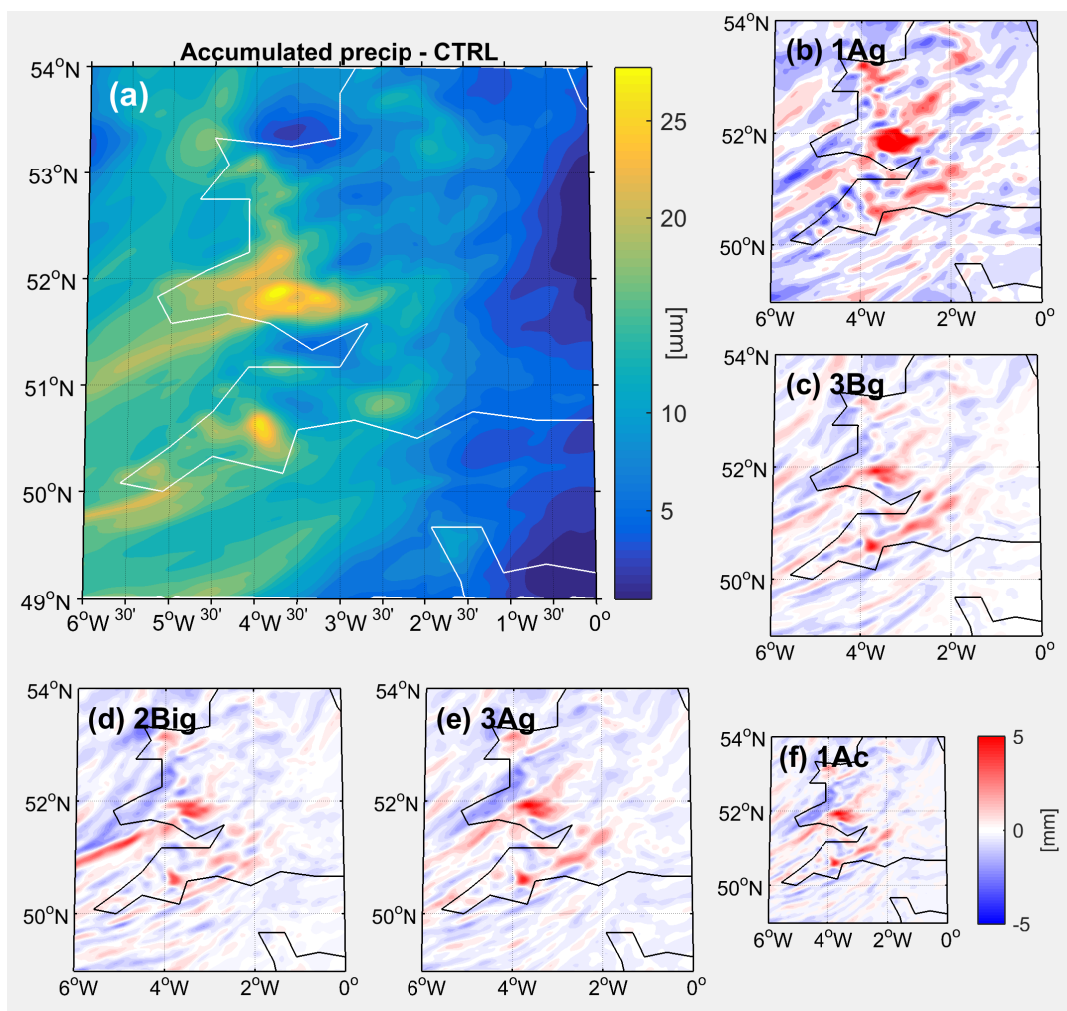
Figure 5. Panel a shows the spatial distribution of accumulated precipitation in the control simulation for a small domain near CFARR at 1800 UTC, as the rainband begins to pass over the UK. Panels b though f show the deviations of accumulated precipitation in five of the simulations with the secondary ice parameterizations in place.

over continental than maritime environments is consistent with observations of other NCFRs (Viale et al., 2013). In panels b through f, deviations from the control simulation field are shown and are largest in those regions where the magnitude of P_{tot} is largest. With magnitudes of up to 5 mm, these deviations represent 20% of the signal. Particularly for two small continental regions at (52°N, 4°W) and (51°N, 3°W) and for the 1Ag simulation, P_{tot} with secondary ice active is 20% larger than the control run value. We emphasize that these P_{tot} deviations are calculated using an average of 10 ensemble runs, so that the signal reflects the change in microphysics not numerics.

Regions of positive P_{tot} deviation are spatially followed by negative P_{tot} deviation and vice versa. This banding appears in the absolute P_{tot} field of panel a as well and reflects convective structure: vertical motion is strongest in the rainband

leading edge, but also preceded and proceeded by weaker convection. Interestingly then, additional ice generation increases the magnitude of these oscillations in convective precipitation. The regions of upward motion and precipitation generation are enhanced, as are the adjacent downdraft regions. There is a similar patterning in fall streak data from the Doppler radar as well (see Crosier et al. (2014), their Figure 5c).

5   As in Figure 3, the impact of adjusting $\aleph_{RS}$ can be seen here between 1Ag in panel b and 1Ac in panel f. The fragment number parameter shifts the magnitude rather than the spatial distribution of the deviations. Regions of positive versus negative deviation overlap, but are about two times larger in magnitude for the 1Ag simulation than the 1Ac one. This result favors the red pathway in Figure 1, whereby the Bergeron process activates at higher ICNC and lower supersaturation and grows crystals to sedimentable size. A final point is that the deviations are not so different between the simulations with droplet shattering in

10   panels b, e, and f and those with ice-ice collisional breakup in panels c and d, suggesting that rime splintering is responsible for much of the change in P_{tot}.

Deviations in $\dot{P}$ (Fig. S1) exhibit much of the same behavior as the P_{tot} field. The highest and lowest deviations fall along the comma shaped curve of the rainband, apparent also in Figure 3. The P_{tot} 'hotspots' at (52°N, 4°W) and (51°N, 3°W) mentioned above reappear, but with 'coldspots' in between. These spots are the result of an NCFR structure with cores

15   of convective precipitation surrounded by more stable areas called gap regions (James and Browning; Hobbs and Persson, 1982; Crosier et al., 2014). The addition of the secondary ice parameterizations both invigorates the convective regions and corresponding precipitation and strengthens the gap downdrafts and corresponding drying. Increasing the fragment number $\aleph_{RS}$ from 1Ac to 1Ag enhances these effects again, and the largest deviations again occur over the continents and due to rime splintering.

20   Finally in Figure 6, we show the simulated and observed time series of precipitation rate in color and black respectively for the same domain near CFARR between 1700 and 2200 UTC. Observations come from the Met Office C-band NIMROD System of rain radars at 5 km spatial and 15 min temporal resolution. The domain-mean values and standard deviation envelopes are shown for both. In panel a, the standard deviation of mean values in a 1 degree longitude-1degree latitude box (1-2°W, 51-52°N) around CFARR is used, whereas in panel b, the mean standard deviation over the 10-simulation ensemble is used. The

25   first can be understood as spatial variance and the second as numerical, and the first is much larger. Because the rainband is so narrow, this is especially true at later times during its passage: the intense precipitation may extend over only 10 kilometers or less, while the small domain around CFARR is still about 50 kilometers by 50 kilometers.

Spatial variance aside, the simulations do not capture the rainband narrowness well in the time series. There is a broad increase in precipitation rate from about 1900 UTC through 2100 UTC, but not the sharp increase to 40 mm h^{-1} as in the

30   observations. The simulations reproduce at most 75% of the magnitude of the maximum $\dot{P}$ and all fall within the spread of one another. This similarity of the simulated series upon spatial averaging may be expected because of the finer-scale rainband structure discussed above, but the averaging is retained for a more robust trend. And in spite of this, the mean $\dot{P}$ remains closest to the observations in the 1Ac and 1Ag simulations with droplet shattering, followed by the 3Bg and 2Big ones with collisional breakup, and lastly the control simulation. This 'hierarchy' of simulations is the same as for ICNCs from Figure 4c.
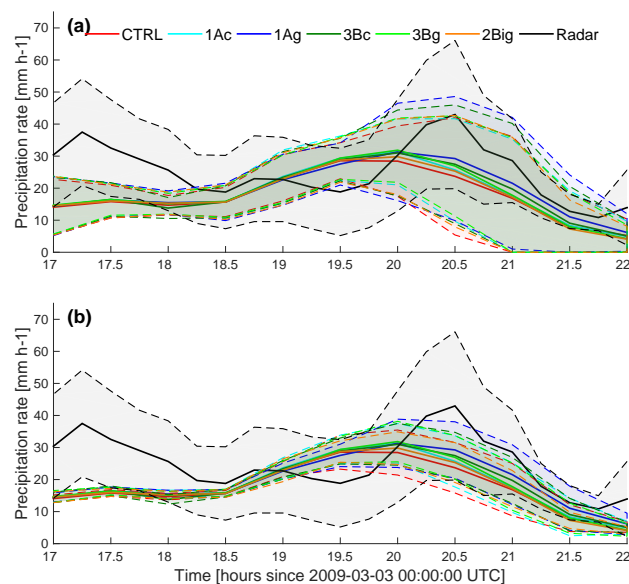
Figure 6. Time series of precipitation rate, both from the UK NIMROD rain radar in black and from various simulations in color for a small domain around CFARR from 1700 to 2200 UTC. For all traces, the mean is shown with an envelope of plus-minus a standard deviation. In panel a, the standard deviation is calculated over the small spatial domain, and in panel b, the standard deviation is calculated over the 10-member ensemble.

5 Discussion

From the time series of N_{ice} in Figure 4, we can estimate secondary ice production rates (Fig. S2). The rates calculated from simulated N_{ice} vary widely, even with extensive smoothing, because the time series constructed in Figure 4 uses the value closest in space and time to the observations and hence often has plateaus of the same N_{ice}. Nevertheless, we can get an

5   order-of-magnitude estimate with a simple finite difference, and the rates from observations are relatively more continuous with smoothing.

From the 1Ag simulation, quite high production rates of up to $50 \, \mathrm{L}^{-1} \, \mathrm{s}^{-1}$ are generated over periods of 5 to 10 minutes early on. The other simulations produce maximum rates of $5 \, \mathrm{L}^{-1} \, \mathrm{s}^{-1}$ around 1930 and 2000 UTC, while the observations produce up to $2.5 \, \mathrm{L}^{-1} \, \mathrm{s}^{-1}$ around 1920 UTC. When there is no spatial averaging as in Figure 3, production rates from secondary

10   ice production alone are as high as $25 \, \mathrm{L}^{-1} \, \mathrm{s}^{-1}$ ($10^5 \, \mathrm{L}^{-1} \, \mathrm{h}^{-1}$) in certain regions. Outside a few peaks in ice generation, the production rate stays around $10^{-2} \, \mathrm{L}^{-1} \, \mathrm{s}^{-1}$. If the observed peak production rate of $2.5 \, \mathrm{L}^{-1} \, \mathrm{s}^{-1}$ lasts for 2 minutes, it will generate an ICNC of $300 \, \mathrm{L}^{-1}$. And if we assume a sedimentation rate of $10^{-6} \, \mathrm{g} \, \mathrm{ice} \, (\mathrm{kg \, air})^{-1} \, \mathrm{s}^{-1}$, equivalent to about 0.25 $\mathrm{L}^{-1} \, \mathrm{s}^{-1}$ for small crystals, the cloud will last for 20 minutes thereafter. If the air is not quiescent, the peak production could be reinvigorated and the lifetime elongated.

The calculated production rates from observations tend to be in agreement with other values in the literature, while those from the simulations are on the high side. Based upon measurements taken over Montana, California, and Florida, Harris-Hobbs and Cooper (1987) estimated ice production rates in cumulus clouds with a difference in ICNC at two sizes normalized by the

5   growth time between those sizes. The majority of their measured and predicted production rates fell between 0.001 and 0.1 L^{-1} s^{-1}, although their probes were probably subject to shattering artifacts (Field et al., 2017). Using the same methodology, Taylor et al. (2016) calculate ice production rates of 0.11 L^{-1} s^{-1} in a dynamic mixed-phase cloud over the southwestern United Kingdom with up- and downdrafts in the ±3 m s^{-1} range and ICNC around 50 L^{-1}. For a more quiescent and glaciated cloud, with updrafts of about 1 m s^{-1} and ICNC up to 270 L^{-1}, they calculate a slightly higher production rate of 0.14 L^{-1}

10   s^{-1}. Mossop (1976) observed ice production rates of 100 s^{-1} at 1.8 m s^{-1} and 200 at 2.4 m s^{-1}, both at -5°C in their cubic meter cloud chamber. Despite these lower production rates, these lasted for as long as 30 minutes.

In mixed-phase parcel model simulations, we have also calculated slower but longer-lasting secondary ice production rates than in these mesoscale simulations (Sullivan et al., 2017, 2018). In simulations that include rime splintering and ice-ice collisional breakup, the model generates about 0.001 L^{-1} s^{-1} when a description of ice non-sphericity is included. But again,

15   these rates last for much longer than those shown in Figure S2, up to 20 minutes. This dichotomy of larger, shorter-lived and smaller, longer-lived production rates in different simulations can be attributed to the representation of the largest hydrometeors, which are crucial both to secondary ice production and precipitation processes. The parcel model contains only six size bins and so does not capture the tail of the size distribution present in the COSMO simulations. Inclusion of hydrometeor number from these tails will enhance the secondary ice production rates, i.e. the tendencies in Equations 1, 4, and 7. But it also enhances

20   the sedimentation rates, so that that multiplication feedbacks (like that shown in green in Figure 1) will be limited in their efficiency.

We have also used parcel model simulations to comment on the relative importance of droplet shattering and ice-ice collisional breakup. Sullivan et al. (2017) found that the dominance of rime splintering versus collisional breakup was determined by timing of large hydrometeor formation in the liquid versus ice phase. Given the relatively low graupel and hail numbers

25   for this cold frontal rainband (Crosier et al., 2014), it is to be expected then that the rime splintering parameterization is most influential on P_{tot} (Section 4.2). The analogous $N_{i,sec}$ field for ice-ice collisional breakup (Figure S3) is about two orders of magnitude less than those shown for droplet shattering in Figure 3. These lower magnitudes reflect to some extent the "self-limiting nature" of ice-ice collisional breakup as well because ice hydrometeors must be consumed to generate them in this process. The absence of a defined rainband structure in Figure S3 corroborates the idea of Sullivan et al. (2018) that secondary

30   ice production processes involving the liquid phase rely more heavily on dynamical "sweet spots" than those involving just the ice phase. Higher enhancement and dynamical dependence of the processes involving the liquid phase should be even more true for simulations at higher spatial resolutions: convection would be better resolved and higher liquid water contents would be generated.

6 Summary

New frozen droplet shattering and ice-ice collisional breakup parameterizations have been developed and implemented into the regional COSMO weather model. We performed several simulations of a cold frontal rainband, observed during the APPRAISE campaign over the UK, with adjustments to the new parameterization formulations. With these runs, we have shown the following:

1. *ICNC generated by secondary production processes can be as large as those from primary nucleation, but in limited domains near convective leading edges where large hydrometeors are present.*

   The new parameterizations calculate $N_{i,sec}$ of up to 10^5 L^{-1} per half hour, values on the order of the primary nucleation tendency, in localized regions. These localized regions are characterized by convective updrafts and by optimal temper-

10 atures that maximize parameters like $\aleph_{BR}$ or p_{DS}. The role of the convective updraft is two-fold, both to generate a supersaturation that forms and grows a large hydrometeor and then to loft that hydrometeor to the optimal temperature zone.

2. *ICNCs greater than 50 L^{-1} are still significantly underestimated with the addition of secondary production parameterizations.*

   From altitudinal profiles, these underestimates are concentrated at altitudes between about 2 and 4 km, where the sec-

15 ondary production processes should be active. In time series, sudden increases or decreases in ICNC are well-captured but their magnitude remains about an order of magnitude too small. The combination of processes or a feedback between them may be missing in the current formulations, or fragment number parameters may be underestimated, although the latter seems unlikely from laboratory estimates. Nonetheless, addition of the secondary ice parameterizations moves the ICNC magnitudes in both vertical and temporal distributions toward the observed values.

3. *The variation between convective precipitation regions and neighboring quiescent ones is intensified by the addition of secondary ice production.*

   The addition of secondary ice systematically increases accumulated precipitation or precipitation rate in regions where these values are largest. The magnitude of these increases can be up to 20% of the signal, but again is very localized, and reduction in P_{tot} and $\dot{P}$ occur in adjacent gap regions. The same effect occurs in both the droplet shattering and

25 ice-ice collisional breakup simulations, meaning that rime splintering is the most influential process for precipitation formation in this particular case. Adjustments in fragment number do not alter the spatial distribution of the effect, only its magnitude. Inclusion of secondary ice parameterizations also brings the simulated maximum precipitation intensity closer to the observed value, although this change is less pronounced and the maximum $\dot{P}$ is still underestimated by 25%.

30 **7 Code availability**

The updated subroutine for the Seifert and Beheng two-moment scheme within the larger COSMO model is available upon request, as are NetCDF4 output files from all sensitivity tests.

8 Data availability

The UK 1 km-resolution NIMROD radar data are available through the Met Office Centre for Environmental Data Analysis
5 at http://catalogue.ceda.ac.uk/uuid/82adec1f896af6169112d09cc1174499. Filtered CIP-15 ICNC data from the 3 March 2009 flight are available upon request, and their corresponding latitude, longitude, and altitudes are available through CEDA at http://data.ceda.ac.uk/badc/faam/data/2009/b433-mar-03/core_processed.

Appendix A: Rain freezing parameterization

Within the Seifert and Beheng two-moment scheme, the number of freezing droplets is calculated with the stochastic model of
10 Bigg (1953):

$$\ln(1 - P_{freez}) = -\int_0^t V_R J_{het} dt, \tag{A1}$$

$$= -\frac{\pi}{6} \int_0^t D_R^3 J_{het} dt \tag{A2}$$

where the heterogeneous nucleation coefficient is defined as $J_{het} = b_{het} \exp(a_{het} \Delta T - 1)$ and ΔT is the supercooling. We use a_{het} of 0.65 and b_{het} of 200 as in Barklie and Gokhale (1959). Then the number of freezing droplets per time is given by

15 $$\frac{\partial N_{freez}}{\partial t} = -N_R \bar{x}_R J_{het} \tag{A3}$$

where N_R is the raindrop number and $\bar{x}_R$ is the mean mass per raindrop.

Appendix B: Hydrometeor size distributions and collision integrals

The generalized Γ size distribution is used for the hydrometeor size distributions within the Seifert and Beheng two-moment scheme:

20 $$f(x) = A x^\nu \exp(-\lambda x^\mu) \tag{B1}$$

where $(\nu + 1)/\mu$ is the shape parameter, λ the rate parameter of the distribution, and x is hydrometeor mass. Then the number of particles of type j that are collected by type k is given by

$$\left.\frac{\partial N_j}{\partial t}\right|_{coll,jk} = -\int\limits_0^\infty \int\limits_0^\infty f_j(x_j) f_k(x_k) K_{jk}(x_j, x_k) dx_j dx_k \tag{B2}$$

where K_{jk} is the collection kernel, the product of the collisional cross section, a collection efficiency, and a differential settling velocity:

$$5 \quad K_{jk}(x_j, x_k) = \frac{\pi}{4}[D_j(x_j) + D_k(x_k)]^2 E_{jk}(x_j, x_k)|v_j(x_j) - v_k(x_k)| \tag{B3}$$

To obtain the analytical expression for the collision integral in Equation 6, the collection efficiency is assumed to be independent of particle sizes: $E_{jk}(x_j, x_k) \approx \overline{E_{jk}}$. The particle diameter is assumed to relate to particle mass through a power law expression: $D_j(x_j) = a_j x_j^{b_j}$. And the differential settling velocity is approximated by a characteristic difference: $|v_j(x_j) - v_k(x_k)| \approx \overline{\Delta v_{jk}}$. Then Equation B2 becomes

$$10 \quad \left.\frac{\partial N_j}{\partial t}\right|_{coll,jk} = -\frac{\pi}{4}\overline{E_{jk}}\,\overline{\Delta v_{jk}}\int\limits_0^\infty \int\limits_0^\infty f_j(x_j) f_k(x_k)[D_j(x_j) + D_k(x_k)]^2 dx_j dx_k \tag{B4}$$

Wisner et al. (1972) have solved this equation with the non-dimensional values δ and θ given by

$$\delta_j^\kappa = \frac{\Gamma(\frac{2b_j + \nu_j + 1 + \kappa}{\mu_j})}{\Gamma(\frac{\nu_j + 1}{\mu_j})}\left[\frac{\Gamma(\frac{\nu_j + 1}{\mu_j})}{\Gamma(\frac{\nu_j + 2}{\mu_j})}\right]^{2b_j + \kappa} \qquad \theta_j^\kappa = \frac{\Gamma(\frac{2\beta_j + 2b_j + \nu_j + 1 + \kappa}{\mu_j})}{\Gamma(\frac{2b_j + \nu_j + 1 + \kappa}{\mu_j})}\left[\frac{\Gamma(\frac{\nu_j + 1}{\mu_j})}{\Gamma(\frac{\nu_j + 2}{\mu_j})}\right]^{2\beta_j} \tag{B5}$$

These non-dimensional values and their derivation are given in greater detail in Seifert (2002) and Seifert and Beheng (2006).

Appendix C: Notation

15   γ Decay rate in the fragment number generated from ice-ice collisional breakup

   λ Rate parameter in the generalized Γ distribution

   μ, ν Factors within the shape parameter of the generalized Γ distribution

   σ Standard deviation in the raindrop shattering probability distribution function

   ICNC   In-cloud ice crystal number concentration

20   **INP**   Ice-nucleating particle number

   $N_{i,pri}$ Primarily nucleated ice crystal number concentration

   $N_{i,sec}$ Secondarily produced ice crystal number concentration

N_R Raindrop number

$\aleph_{BR}$ Fragment number from ice-ice collisional breakup per collider (e.g., graupel in *ig or *sg simulations) number

$\aleph_{DS}$ Fragment number from droplet shattering per large droplet number

$\aleph_{RS}$ Fragment number from rime splintering per milligram of rime

p_{DS} Temperature dependent probability that a freezing raindrop shatters

5 P_{freez} Probability that a raindrop freezes versus time according to Bigg (1953)

p_{max} Maximum probability that a freezing raindrop shatters, parameter within p_{DS}

$\dot{P}$ Precipitation intensity

P_{tot} Accumulated precipitation

T_{min} Minimum temperature for ice-ice collisional breakup to occur

10 T_μ Associated temperature for the maximum in the raindrop shattering probability distribution function

V_R Raindrop volume

$\overline{x_R}$ Mean raindrop mass

Author contributions. SCS and CH constructed the parameterizations and chose the case study. SCS implemented the parameterizations in COSMO. CB assisted with model setup and porting, and JC provided campaign data and analysis codes. SCS, CH, and AN analyzed
15 simulation output.

Competing interests. The authors declare that they have no conflict of interest.

Acknowledgements. SCS and CH thank support from the Helmholtz Association through the President's Initiative and Networking Fund (VH-NG-620). SCS and AN acknowledge funding from a NASA Earth and Space Science Fellowship (NNX13AN74H) and NASA MAP grant, as well as the DOE EaSM. JC and the source campaigns for our data were funded by the NERC APPRAISE programme, grant number
20 NE/E01125X/1. All authors wish to thank the Deutscher Wetterdienst (DWD) for providing the COSMO model code as well as the initial and boundary data. In addition, SCS would like to thank Marco Paukert, Isabelle Reichardt, Tobias Schad, Heike Vogel, and Luke Hande for helpful discussion about the COSMO model during a six-month stay at the Institute of Meteorology and Climate Research in Karlsruhe.

References

Aleksić, N.: Precipitation effects of hail suppression in Serbia, Theor. Appl. Climatol., 40, 271–279, doi:10.1007/BF00865978, 1989.

Arkin, P. A. and Meisner, B. N.: The relationship between large-scale convective rainfall and cold cloud over the Western Hemisphere during 1982-84, Mon. Weather Rev., 115, 51–74, doi:10.1175/1520-0493(1987)115<0051:TRBLSC>2.0.CO;2, 1987.

Baldauf, M., Seifert, A., Förstner, J., Majewski, D., and Raschendorfer, M.: Operational convective-scale numerical weather prediction with the COSMO model: Description and sensitivities, Mon. Weather Rev., 139, 3887–3905, doi:10.1175/MWR-D-10-05013.1, 2011.

Barklie, R. H. D. and Gokhale, N.: The freezing of supercooled water drops, 1959.

Bigg, E. K.: The formation of atmospheric ice crystals by the freezing of droplets, Q. J. Roy. Meteorol. Soc., 79, 510–519, doi:10.1002/qj.49707934207, 1953.

Broadley, S., Murray, B., Herbert, R., Atkinson, J., Dobbie, S., Malkin, T., Condliffe, E., and Neve, L.: Immersion mode heterogeneous ice nucleation by an illite rich powder representative of atmospheric mineral dust, Atmos. Chem. Phys., 12, 287–307, doi:10.5194/acp-12-287-2012, 2012.

Buizza, R., Milleer, M., and Palmer, T. N.: Stochastic representation of model uncertainties in the ECMWF ensemble prediction system, Quar. Jour. Roy. Meteor. Soc., 125, 2887–2908, doi:10.1002/qj.49712556006, 1999.

Choularton, T. W., Griggs, D. J., Humood, B. Y., and Latham, J.: Laboratory studies of riming, and its relation to ice splinter production, Quart. J. Roy. Meteor. Soc., 106, 367–374, doi:10.1002/qj.49710644809, 1980.

Clark, P., Choularton, T. W., Brown, P. R. A., Field, P. R., Illingworth, A. J., and Hogan, R. J.: Numerical modelling of mixed-phase frontal clouds observed during the CWVC project, Q. J. R. Meteorol. Soc., 131, 1677–1693, doi:10.1256/qj.03.210, 2005.

Connolly, P. J., Choularton, T. W., Gallagher, M. W., Bower, K. N., Flynn, M. J., and Whiteway, J. A.: Cloud-resolving simulations of intense tropical *Hector* thunderstorms: Implications for aerosol-cloud interactions, Q. J. Meteorol. Soc., 132, 3079–3106, doi:10.1256/qj.05.86, 2006.

Crawford, I., Bower, K. N., Choularton, T. W., Dearden, C., Crosier, J., Westbrook, C., Capes, G., Coe, H., Connolly, P. J., Dorsey, J. R., Gallagher, M. W., Williams, P., Trembath, J., Cui, Z., and Blyth, A.: Ice formation and development in aged, wintertime cumulus over the UK: observations and modelling, Atmos. Chem. Phys., 12, 4963–4985, doi:10.5194/acp-12-4963-2012, 2012.

Crosier, J., Choularton, T. W., Westbrook, C. D., Blyth, A. M., Bower, K. N., Connolly, P. J., Dearden, C., Gallagher, M. W., Cui, Z., and Nicol, J. C.: Microphysical properties of cold frontal rainbands, Q. J. Roy. Meteorol. Soc., 140, 1257–1268, doi:10.1002/qj.2206, 2014.

Dearden, C., Vaughan, G., Tsai, T., and Chen, J.: Exploring the diabatic role of ice microphysical processes in two North Atlantic summer cyclones, Mon. Wea. Rev., 144, 1249–1272, doi:10.1175/MWR-D-15-0253.1, 2016.

DeMott, P. J., Prenni, A. J., Liu, X., Kreidenweis, S. M., Petters, M. D., Twohy, C. H., Richardson, M. S., Eidhammer, T., and Rogers, D. C.: Predicting global atmospheric ice nuclei distributions and their impacts on climate, Proc. Nat. Acad. Sci., doi:10.1073/pnas.0910818107, 2010.

DeMott, P. J., Hill, T. C. J., McCluskey, C. S., Prather, K. A., Collins, D. B., Sullivan, R. C., Ruppel, M. J., Mason, R. H., Irish, V. E., Lee, T., Hwang, C. Y., Rhee, T. S., Snider, J. R., McMeeking, G. R., Dhaniyala, S., Lewis, E. R., Wentzell, J. J. B., Abbatt, J., Lee, C., Sultana, C. M., Ault, A. P., Axson, J. L., Martinez, M. D., Venero, I., Santos-Figueroa, G., Stokes, M. D., Deane, G. B., Mayol-Bracero, O. L., Bertram, V. H. G. T. H., Bertram, A. K., Moffett, B. F., and Franc, G. D.: Sea spray aerosol as a unique source of ice nucleating particles, Proc. Natl. Acad. Sci., 113, 5797–5803, doi:10.1073/pnas.1514034112, 2016.

Doms, G. and Baldauf, M.: A description of the nonhydrostatic regional COSMO-Model. Part II: Physical parameterization, Tech. rep., 2015.

Field, P., Lawson, P., Brown, G., Lloyd, C., Westbrook, D., Moisseev, A., Miltenberger, A., Nenes, A., Blyth, A., Choularton, T., Connolly, P., Bühl, J., Crosier, J., Cui, Z., Dearden, C., DeMott, P., Flossmann, A., Heymsfield, A., Huang, Y., Kalesse, H., Kanji, Z., Korolev, A., Kirchgaessner, A., Lasher-Trapp, S., Leisner, T., McFarquhar, G., Phillips, V., Stith, J., and Sullivan, S.: Chapter 7: Secondary ice production - current state of the science and recommendations for the future, Meteor. Monogr., doi:10.1175/AMSMONOGRAPHS-D-16-0014.1, 2017.

5 Field, P. R., Wood, R., Brown, P. R. A., Kaye, P. H., Hirst, E., Greenaway, R., and Smith, J. A.: Ice particle interarrival times measured with a fast FSSP, J. Atm. Ocean. Tech., 20, 249–261, doi:10.1175/1520-0426(2003)020, 2003.

Field, P. R., Heymsfield, A. J., and Bansemer, A.: Shattering and particle interarrival times measured by optical array probes in ice clouds, J. Atm. Ocean. Tech., 23, 1357–1371, doi:10.1175/JTECH1922.1, 2006.

Glassmeier, F. and Lohmann, U.: Constraining precipitation with susceptibility of warm-, ice-, and mixed-phase clouds with microphysical
10 equations, J. Atm. Sci., 73, 5003–5023, doi:10.1175/JAS-D-16-0008.1, 2016.

Hallett, J. and Mossop, S. C.: Production of secondary ice particles during the riming process, Nature, 249, 26–28, doi:10.1038/249026a0, 1974.

Harris-Hobbs, R. L. and Cooper, W. A.: Field evidence supporting quantitative predictions of secondary ice production rates, J. Atmos. Sci., 44, 1071–1082, doi:10.1175/1520-0469(1987)044<1071:FESQPO>2.0.CO;2, 1987.

15 Heymsfield, A. and Willis, P.: Cloud conditions favoring secondary ice particle production in tropical maritime convection, 71, 4500–4526, doi:10.1175/JAS-D-14-0093.1, 2014.

Heymsfield, A. J.: On measurements of small ice particles in clouds, Geophys. Res. Lett., 34, doi:10.1029/2007GL030951, 2007.

Hobbs, P. V. and Persson, P. O. G.: The mesoscale and microscale structure and organization of clouds and precipitation in midlatitude cyclones. Part V: the substructure of narrow cold-frontal rainbands, J. Atm. Sci., 39, 280–295, doi:10.1175/1520-
20 0469(1982)<0280:TMAMSA>2.0.CO;2, 1982.

Hoose, C. and Möhler, O.: Heterogeneous ice nucleation on atmospheric aerosols: a review of results from laboratory experiments, Atmos. Chem. Phys., 12, 12 531–12 621, doi:10.5194/acpd-12-12531-2012, 2012.

James, P. K. and Browning, K. A.: Mesoscale structure of line convection at surface cold fronts, Q. J. R. Meteorol. Soc., 105, 371–382, doi:10.1002/qj.4971054404.

25 Joyce, R. and Arkin, P. A.: Improved estimates of tropical and subtropical precipitation using the GOES precipitation index, J. Atm. Ocean. Tech., 14, 997–1011, doi:10.1175/1520-0426(1997)014<0997:IEOTAS>2.0.CO;2, 1997.

Khain, A., Rosenfeld, D., and Pokrovsky, A.: Aerosol impact on the dynamics and microphysics of deep convective clouds, Q. J. R. Meteorol. Soc., 131, 2639–2663, doi:10.1256/qj.04.62, 2005.

Knopf, D. A. and Koop, T.: Heterogeneous nucleation of ice on surrogates of mineral dust, J. Geophys. Res., 111,
30 doi:10.1029/2005JD006894, 2006.

Korolev, A.: A study of bimodal droplet size distributions in stratiform clouds, Atm. Res., 32, 143–170, doi:10.1016/0169-8095(94)90057-4, 1994.

Korolev, A. V. and Field, P. R.: Assessment of the performance of the inter-arrival time algorithm to identiy ice shattering artifacts in cloud particle probe measurements, Atm. Meas. Tech., 8, 761–777, 2015.

35 Korolev, A. V., Emery, E. F., Strapp, J. W., Cober, S. G., and Isaac, G. A.: Quantification of the effects of shattering on airborne ice particle measurements, J. Atm. Ocean. Tech., 30, 2527–2553, doi:10.1175/JTECH-D-13-00115.1, 2013a.

Korolev, A. V., Strapp, J. A., Isaac, G. A., and Emery, E.: Improved airborne hot-wire measurements of ice water content in clouds, J. Atm. Ocean. Tech., 30, 2121–2131, doi:10.1175/JTECH-D-13-00007.1, 2013b.

Lasher-Trapp, S., Leon, D. C., DeMott, P. J., Villanueva-Birriel, C. M., Johnson, A. V., Moser, D. H., Tully, C. S., and Wu, W.: A multisensor investigation of rime splintering in tropical maritime cumuli, J. Atm. Sci., 73, 2547–2564, doi:10.1175/JAS-D-15-0285.1, 2016.

Lau, K.-M. and Wu, H.-T.: Climatology and changes in tropical ocean rainfall characteristics inferred from Tropical Rainfall Measuring Mission (TRMM) data (1998-2009), J. Geophys. Res., 116, doi:10.1029/2011JD015827, 2011.

Lawson, R. P., Woods, S., and Morrison, H.: The microphysics of ice and precipitation development in tropical cumulus clouds, J. Atm. Sci., 72, 2429–2445, doi:10.1175/JAS-D-14-0274.1, 2015.

Leisner, T., Pander, T., Handmann, P., and Kiselev, A.: Secondary ice processes upon heterogeneous freezing of cloud droplets, 14th Conf. on Cloud Physics and Atmospheric Radiation, Amer. Meteor. Soc, Boston, MA, 2014.

Lohmann, U.: Anthropogenic aerosol influences on mixed-phase clouds, Curr. Clim. Change Rep., doi:10.1007/s40641-017-0059-9, 2017.

Mason, B. J. and Jonas, P. R.: Evolution of droplet spectra and large droplets by condensation in cumulus clouds, Q. J. Roy. Meteorol. Soc., pp. 23–38, 1974.

McFarquhar, G. M., Um, J., Freer, M., Baumgardner, D., Kok, G. L., and Mace, G.: Importance of small ice crystals to cirrus properties: Observations from Tropical Warm Pool International Cloud Experiment (TWP-ICE), Geophys. Res. Lett., 34, doi:10.1029/2007GL029865, 2007.

Milbrandt, J. A. and Morrison, H.: Parameterization of cloud microphysics based on the prediction of bulk ice particle properties. Part III: Introduction of multiple free categories, J. Atm. Sci., 73, 975–995, doi:10.1175/JAS-D-15-0204.1, 2015.

Möhler, O., Field, P. R., Connolly, P., Benz, S., Saathoff, H., Schnaiter, M., Wagner, R., Cotton, R., Krämer, M., Mangold, A., and Heymsfield, A. J.: Efficiency of the deposition mode ice nucleation on mineral dust particles, Atmos. Chem. Phys., 6, 3007–3021, doi:10.5194/acp-6-3007-2006, 2006.

Möhler, O., Georgakopoulos, D. G., Morris, C. E., Benz, S., Ebert, V., Hunsmann, S., Saathoff, H., Schnaiter, M., and Wagner, R.: Heterogeneous ice nucleation activity of bacteria: new laboratory experiments at simulated cloud conditions, Biogeosci., 5, 1425–1435, doi:10.5194/bg-5-1425-2008, 2008.

Morrison, H. and Milbrandt, J. A.: Parameterization of cloud microphysics based on the prediction of bulk ice particle properties. Part I: Scheme description and idealized tests, 72, 287–311, doi:10.1175/JAS-D-14-0065.1, 2015.

Mossop, S. C.: Production of secondary ice particles during the growth of graupel by riming, Q. J. Roy. Meteor. Soc., 102, 45–57, doi:10.1002/qj.49710243104, 1976.

Mossop, S. C.: Secondary ice particle production during rime growth: The effect of drop size distribution and rimer velocity, Q. J. R. Meteorol. Soc., 111, 1113–1124, doi:10.1002/qj.49711147012, 1985.

Mülmenstädt, J., Sourdeval, O., and Delano e, J.: Frequency of occurrencee of rain from liquid-, mixed-, and ice-phase clouds derived from A-Train satellite retrievals, Geophys. Res. Lett., 42, 6502–6509, doi:10.1002/2015GL064604, 2015.

O'Sullivan, D., Murray, B. J., Ross, J. F., Whale, T. F., Price, H. C., Atkinson, J. D., Umo, N. S., and Webb, M. E.: The relevance of nanoscale biological fragments for ice nucleation in clouds, Sci. Rep., 5, doi:10.1038/srep08082, 2015.

Phillips, V., DeMott, P., and Andronache, C.: An empirical parameterization of heterogeneous ice nucleation for multiple chemical species of aerosol, J. Atmos. Sci., 65, 2757–2783, doi:10.1175/2007JAS2546.1, 2008.

Rosenfeld, D. and Gutman, G.: Pollution and clouds, Physics World, 14, 259–283, 2001.

Segal, Y. and Khain, A.: Dependence of droplet concentration on aerosol conditions in different cloud types: Application to droplet concentration parameterization of aerosol conditions, J. Geophys. Res.-Atmos., 111, doi:10.1029/2005JD006561, 2006.

Seifert, A.: Parametrisierung wolkenmikrophysikalischer Prozesse und Simulation konvektiver Mischwolken, Ph.D. thesis, Universität Karlsruhe, 2002.

Seifert, A. and Beheng, K. D.: A two-moment cloud microphysics parameterization for mixed-phase clouds. Part I: Model description, Meteorol. Atmos. Phys., 92, 45–66, doi:10.1002/2014JD021917, 2006.

Sud, Y. C. and Walker, G. W.: Influence of ice-phase physics of hydrometeors on moist-convection, Geophys. Res. Lett., 30, doi:10.1029/2003GL017587, 2003.

Sullivan, S., Hoose, C., and Nenes, A.: Investigating the contribution of secondary production to ice crystal number concentrations, J. Geophys. Res., doi:10.1002/2017JD026546, 2017.

Sullivan, S. C., Kiselev, A., Leisner, T., Hoose, C., and Nenes, A.: Initiation of secondary ice production in clouds, Atmos. Chem. Phys., 18, 1593–1610, doi:10.5194/acp-18-1593-2018, 2018.

Takahashi, T., Nagao, Y., and Kushiyama, Y.: Possible high ice particle production during graupel-graupel collisions, J. Atmos. Sci., 52, 4523–4527, doi:10.1175/1520-0469, 1995.

Taylor, J. W., Choularton, T. W., Blyth, A. M., Liu, Z., Bower, K. N., Crosier, J., Gallagher, M. W., Williams, P. I., Dorsey, J. R., Flynn, M. J., Bennett, L. J., Huang, Y., French, J., Korolev, A., and Brown, P. R. A.: Observations of cloud microphysics and ice formation during COPE, Atmos. Chem. Phys., 16, doi:10.5194/acp-16-799-2016, 2016.

Vardiman, L.: The generation of secondary ice particles in clouds by crystal-crystal collision, J. Atmos. Sci., 35, 2168–2180, doi:10.1175/1520-0469, 1978.

Viale, M., Houze, R. A., and Rasmussen, K. L.: Upstream orographic enhancement of a narrow cold-frontal rainband approaching the Andes, Mon. Weather Review, 141, 1708–1730, doi:10.1175/MWR-D-12-00138.1, 2013.

Wildeman, S., Sterl, S., Sun, C., and Lohse, D.: Fast dynamics of water droplets freezing from the outside in, Phys. Rev. Lett., 118, doi:10.1103/PhysRevLett.118.084101, 2017.

Wisner, C., Orville, H. D., and Myers, C.: A numerical model of a hail-bearing cloud, J. Atm. Sci., 29, 1160–1181, doi:10.1175/1520-0469(1972)029>1160% 3AANMOAH<2.0.CO% 3B2, 1972.

Yano, J.-I. and Phillips, V. T. J.: Ice-ice collisions: an ice multiplication process in atmospheric clouds, J. Atmos. Sci., 68, 322–333, doi:10.1175/2010JAS3607.1, 2011.

Zhu, H., Maloney, E., Hendon, H., and Stratton, R.: Effects of the changing heating profile associated with melting layers in a climate model, Q. J. Roy. Meteorol. Soc., doi:10.1002/qj.3166, 2017.